Laser engraving optimization for achieving smooth sidewalls

Aurélien Sikora, Gaëlle Coustillier, Thierry Sarnet, Marc Sentis

Laser engraving optimization for achieving smooth sidewalls

AURELIEN SIKORA,* GAËLLE COUSTILLIER, THIERRY SARNET, MARC SENTIS

Aix Marseille Univ, CNRS, LP3, Marseille, France

**Corresponding author: sikora@lp3.univ-mrs.fr*

Highlights

- **Sidewall roughness of laser engraved cavities depends highly on the crater overlap.**
- **Laser engraving induces a periodic structuring of the sidewall surface.**
- **The roughness can be tuned by varying the crater overlap and size.**
- **This behavior is well explained by a simple geometrical model.**
- **Several factors prevent the formation of super smooth (nm scale) sidewall surface.**

Abstract

The surface roughness of picosecond laser micromachined sidewalls in silicon is investigated theoretically and experimentally by varying the laser fluence, the focal spot size and the crater overlap. It is shown that the precise spot positioning and the repeated ablation induce a periodic structuring of the sidewall surface. The roughness measured by confocal microscopy along the laser scanning direction (R_aX), can be decreased by increasing the crater overlap and the focal spot size. This behaviour, confirmed using two different lasers, can be explained by a simple geometrical model. However, above an optimal crater overlap of approximately 80%, the surface roughness increases again. The sources of this limitation are discussed. The roughness measured along the beam propagation direction (R_aY) is minimal around a crater overlap of 80% as well. Varying the spot size does not significantly change R_aY but impacts on the curvature of the sidewall. Moreover, it is shown that once the sidewall is fully formed, its surface roughness is barely dependent on the number of laser scanning passes.

Keywords

Laser micromachining; sidewall; surface roughness; picosecond laser; silicon

Graphical abstract

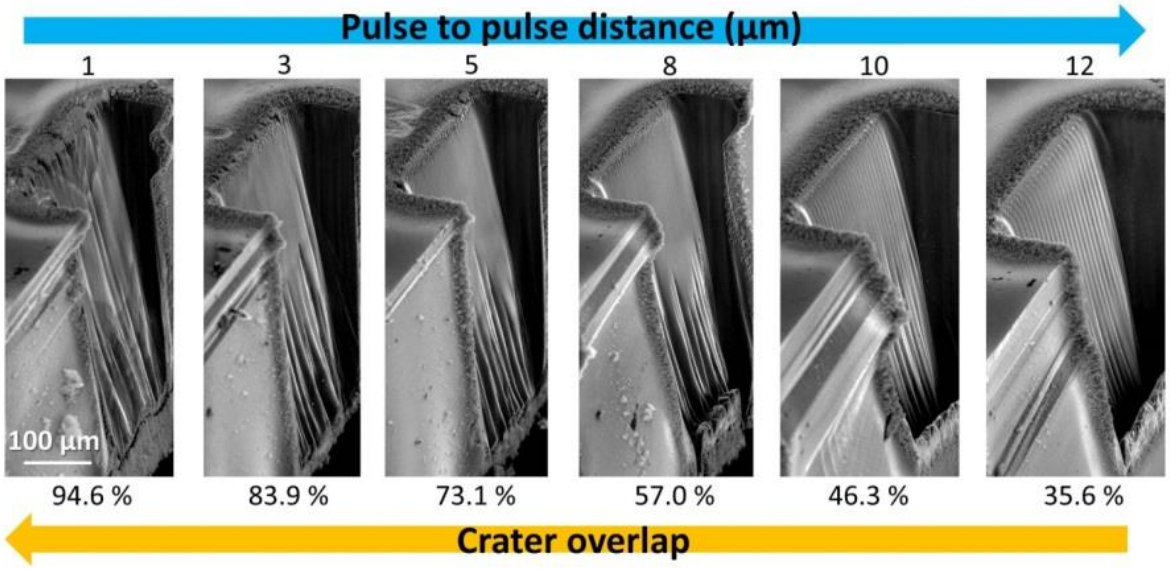

1. Introduction

As a contactless and maskless method generating a reduced heat affected zone compared to nanosecond laser, ultrafast laser micromachining is widely used for rapid prototyping and materials processing [1]. For many applications, there is a strong need to produce highly smooth sidewalls but today, most research and development works is devoted to study and control Laser Induced Periodic Surface Structures (LIPPS) occurring at the surface of the cavity bottom [2]. For examples, smooth sidewalls are required to : i) reduce the post processing polishing time by focus ion beam (FIB) after laser sample preparation [3], ii) elaborate low liquid friction and low adhesion microchannels for microfluidics [4, 5], iii) minimize the scattering losses in waveguides [6, 7], iv) improve the performance of micro heat pipes [8], and v) improve the mechanical properties of silicon dices [9, 10]. A laser based technology allowing to obtain very smooth surfaces (Ra of ~3 nm) already exists [7, 11, 12] but it involves melting of a significant volume of material, which is absolutely not acceptable for certain applications, i.e. sample preparation, in which no defect should be generated. In addition, as it requires a melting step, this method is not applicable to all materials, for example thermosetting plastics. Moreover the success of this process depends on the material properties: surface tension, viscosity, etc. [11].

In this study, we investigate picosecond laser micromachining of cavity sidewalls in silicon, one of the major materials used in the aforementioned applications. Sidewall micromachining of silicon was mostly studied for MEMS fabrication [13, 14] and wafer dicing [9, 10, 15]. For example, nanosecond micromachining conditions were improved using the Taguchi method and a surface roughness of 0.37 µm was achieved for a laser pulse overlap of 80% [13]. However, in this study, the roughness was measured at 3 different sidewall locations and not on the whole surface, the obtained parameters were not guaranteed as optimal and such a statistical method does not allow a convenient understanding of the results. Concerning the wafer dicing investigations, it was shown using a nanosecond laser that increasing the laser beam overlap improves the quality of the edge [16]. In addition, an investigation performed using high repetition rate laser sources showed that the sidewall

roughness is strongly dependent on the pulse duration [9]. An average surface roughness of 335 nm was obtained using a pulse duration of 214 fs at repetition rate of 4.33 MHz.

So far, to the best of our knowledge, no parametric study aiming at minimizing the roughness of picosecond laser micromachined sidewalls in silicon has been performed. In this regime, it has been shown that the heat affected zone is very reduced compared to nanosecond laser machining [3]. Thus, for picosecond pulses, the melted layer is thinner and the machined surface will be more representative of the geometric parameters of the process. Hereinafter, we investigate the effects of the laser pulse overlap, focal spot size and fluence on the roughness of micromachined sidewalls. The experimental results are discussed in conjunction with a simple geometrical model. By using two different picosecond lasers, we highlight a general roughness evolution behavior when varying the parameters.

2. Materials and methods

300 µm wide and 100 to 500 µm deep cavities are engraved in air on the edge of cleaved 525+/-25 µm thick phosphorous doped silicon wafers (Si-Mat) oriented <100> with a resistivity of 1-10 Ω.cm. The number of laser pulses per area is kept constant when changing the laser beam overlap. When varying the fluence, the number of pulses per area is arbitrarily chosen as inversely proportional to the pulse energy in order to keep an approximately constant cavity depth. Experiments are performed with a Hylase-25-SHG (Fianium) and a Hegoa laser (Eolite) in association with a galvanometer scanner (Scanlab, Intelliscan 14). The laser features are detailed in Table 1. The laser micromachining station is fully described elsewhere [17]. At 343 nm, the laser incidence angle is kept at 90° by using a telecentric objective. At 532 nm, a non telecentric objective is used but the scanning area is small enough (300x100 µm^2) to consider that the incidence angle variation is negligible. The laser waist sizes are changed with an optical telescope. The focal point is set on the surface of the wafer. The focal spot sizes are estimated using the diameter regression method [18]. Machining conditions (fluence and laser scanning method) are chosen such as the obtained sidewalls are almost free of debris. Therefore, the applied fluence is high enough to remove the debris during the engraving [3] and the laser beam is scanned parallel to the wafer edge such as the beam scanning ends on the sidewall.

Table 1 : laser parameters.

Laser	**Hylase**	**Hegoa**		
Wavelength (nm)	532	343		
Pulse duration (ps)	8	50		
Repetition rate *f* (kHz)	30	20		
Max. power delivered on samples (W)	~1.34	~0.11		
Focal spot radius ω_0 at 1/e^2 (µm)	~15	~5	~9	~13

Max. fluence (J.cm^{-2})	~6.3	~7	~2.2	~1

Scanning electron microscope (SEM) images are acquired with a JSM-6390 microscope (JEOL). The crater diameters and sidewall roughness were measured with a confocal microscope (Leica, DCM 3D). Topological data were acquired along an area of ~ 85 x 75 µm^2 just below the wafer surface using with a spatial resolution (x and y) of 0.33 µm and Δz below 3 nm (objective x50). The roughness is calculated using the formula: $R_a = \frac{1}{n} \sum_{i=1}^{n} |z_i - \bar{z}|$ with $\bar{z}$ the average value of the profile height [19]. In this work, depending on the orientation of the scanned line, two different roughness values are characterized: R_aX and R_aY, for which the topological data are acquired along the *x* and *y* axis respectively. In order to consider only the sidewall and not the interface with the wafer surface, the average roughness was calculated for *y* between 10 and 85 µm.

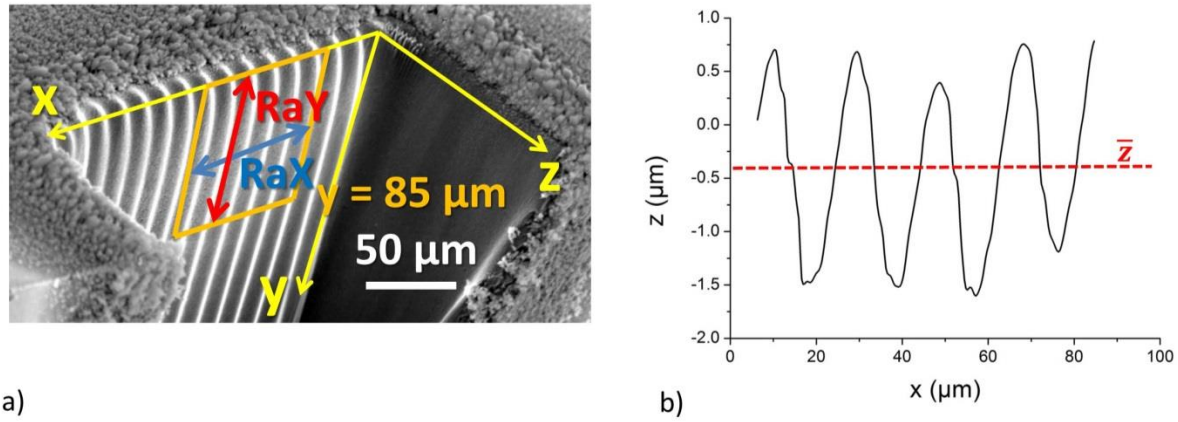

Figure 1 : a) Example of laser engraved cavity (532 nm, 6 J.cm^{-2} and 20% pulse overlap). The roughness is measured in the squared area (orange). b) Example of measured profile along the X direction. The dashed line represents the average height $\bar{z}$.

3. Results and discussion

3.1. Sidewall roughness along the scanning direction (R_aX)

3.1.1. Geometrical model for R_aX

In order to investigate the roughness of the sidewalls induced during laser micromachining, we at first developed a simple geometrical model with the aim of pointing out relevant parameters which may affect the evolution of the roughness. In summary, we assume that the sidewall profile is defined by the shape of the ablated craters (see Figure 2a). Thus, the maximum profile height, i.e. the peak to valley distance, depends on the spacing between the laser pulses, i.e. the pulse to pulse distance. Then, assuming that the craters are circular, the average height of the profile and the resulting roughness can be calculated.

Assuming a circular Gaussian beam shape, the crater diameter *d* can be expressed has followed [18, 20]:

$$d^2 = 2{\omega_0}^2 \ln\left(\frac{F}{F_{th}}\right) \qquad (1)$$

with ω_0 the measured beam waist radius, F the applied laser fluence defined as the as ratio between the pulse energy E and the beam waist area $\pi\omega_0^2$, and F_{th} the ablation fluence threshold.

The height z of the profile varies following the circle equation:

$$z = b - \sqrt{\frac{d^2}{4} - (x-a)^2} \qquad (2)$$

with the circle center coordinates (a,b). b is chosen such as the circle is tangential to the x axis. Thus, in the following, b=d/2. We can show that two circles with centers separated by a distance p (i.e. center coordinates (0,d/2) and (p,d/2)) cross each other at a distance p/2. The peak to valley height PV is consequently given by z(p/2):

$$PV = \frac{d}{2} - \sqrt{\frac{d^2 - p^2}{4}} \qquad (3)$$

Thus, it appears analytically that the laser machined surface profile becomes flatter when increasing the crater diameter d and reducing the pulse to pulse distance p. Knowing the crater size and the inter pulse distance p, the crater overlap (CO) can be calculated as followed:

$$CO\ (\%) = 100 \times \left(1 - \frac{p}{d}\right) \qquad (4)$$

p is given by the ratio v/f with v the scanning velocity and f the laser repetition rate.

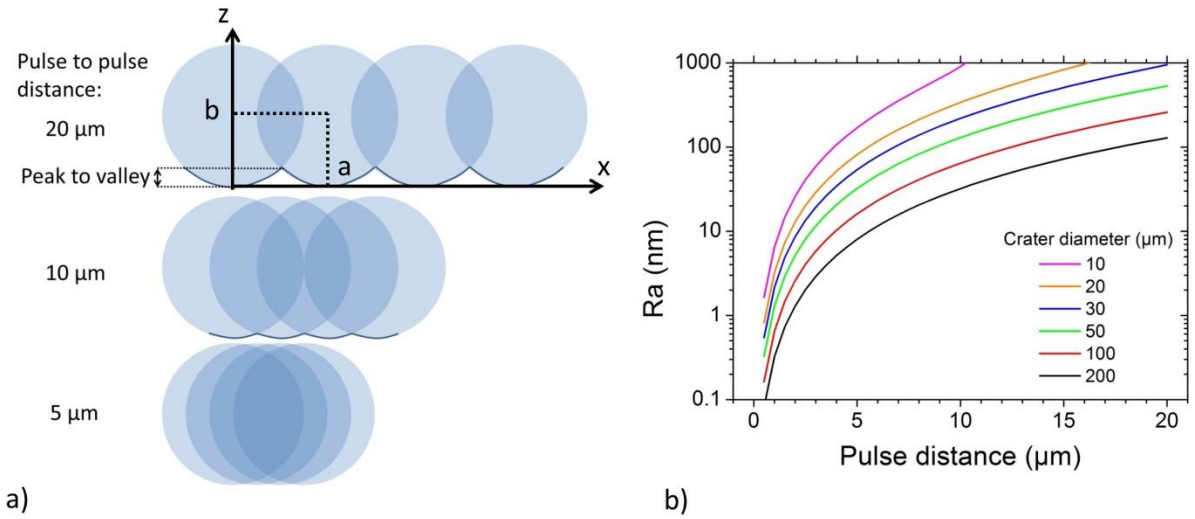

Figure 2 : a) Schematic representation showing the effect of the pulse to pulse distance (overlap) on the peak to valley height. b) Evolution of the theoretical roughness (R_aX) as a function of the pulse to pulse distance for different crater sizes.

Knowing the variation of z with x, the roughness R_aX can be calculated as well using the following equation:

$$RaX = \frac{1}{p/2}\int_0^{p/2} |z - \bar{z}| dx \qquad (5)$$

with $\bar{z}$ the average value of z between 0 and p/2. The variation of the roughness with the pulse to pulse distance for different crater diameters is shown in Figure 2b. It confirms that R_aX increases with the pulse distance and when reducing the crater diameter. According to this geometrical model, sub nanometer roughness should be obtained by a simple reduction of the pulse to pulse distance, typically below 1 µm.

This proposed model is tested by engraving cavities with different pulse to pulse distances (0.25 to 20 µm). The influence of the crater diameter on the roughness is studied by varying the applied fluence and the beam waist size.

3.1.2. Effect of crater overlap, fluence and beam size

The effect of the crater overlap is investigated by engraving cavities with different pulse to pulse distances. The next figure shows SEM images of sidewalls engraved using the Hylase laser.

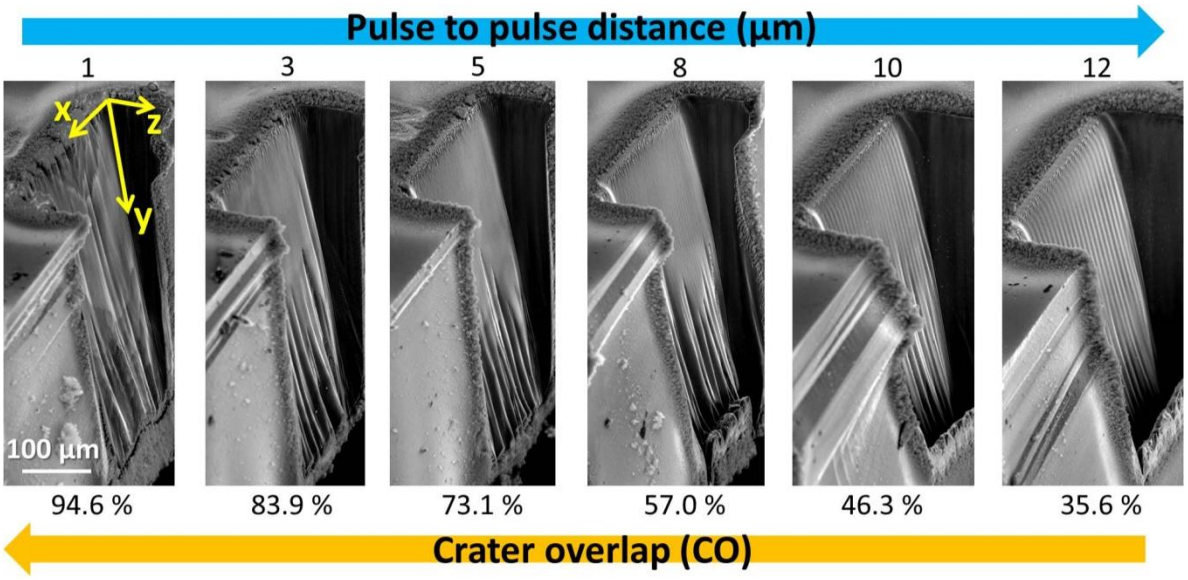

Figure 3 : SEM images of sidewalls engraved in silicon at 2.6 J.cm^{-2} (532 nm, 30 kHz and 2680 laser pulses/area) for different crater overlaps (d ≈ 30 µm).

For large CO (94.6 %), the sidewall appears very irregular and with randomly distributed structures. When decreasing CO, first, the surface looks smoother while for lower values (CO< 46.3 %) a periodic structuring becomes increasingly visible. In order to better characterize the topology of the sidewalls, the measured profiles $z(x)$ are averaged along the whole surface, i.e. between y = 10 and 85 µm, and the resulting profiles are shown in figure 4.

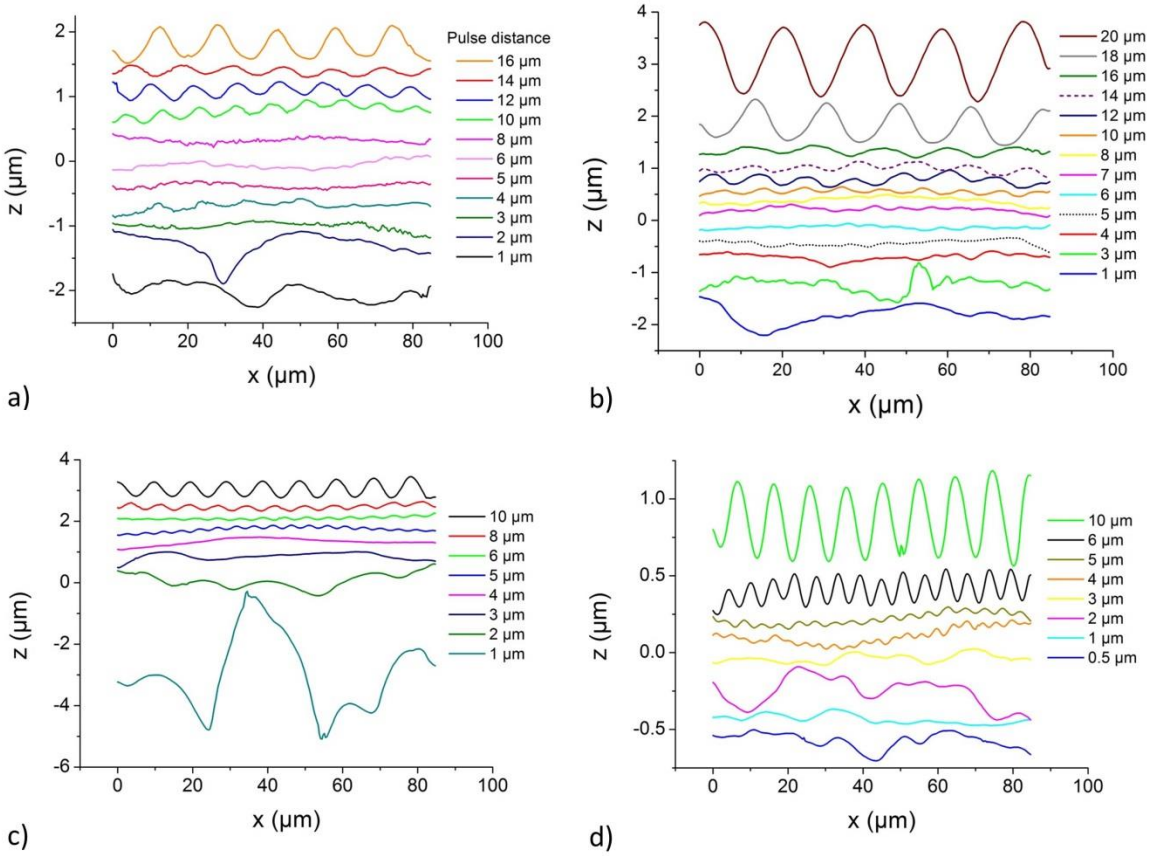

Figure 4 : Average sidewall profiles after laser engraving at wavelength of 532 nm and 30 kHz repetition rate and by applying fluences of 2.6 J.cm^{-2} (a) and 6 J.cm^{-2} (b); at wavelength of 343 nm and 200 kHz repetition rate, 4.3 J.cm^{-2} (c) and 2.1 J.cm^{-2} (d) for different pulse to pulse distances. The curves have been vertically translated in order to facilitate the reading.

The profiles confirm the trend shown by the SEM images. The periodicity progressively disappears as CO increases. The measurement of the distance between each peak shows that the periodicity matches the pulse to pulse distance with an average shift varying between 0.4 and 6.7%. Below a certain pulse to pulse distance (~5 µm), aperiodic structures appear and the quality of the sidewall deteriorates. Sidewall profile measurements performed with other fluences and beam sizes (data not shown) confirm this general trend. The matching between the measured peak amplitude and the expected PV deduced from the laser parameters is discussed later by comparing the roughness values.

In order to complete the study, the roughness of the sidewalls is measured and compared to the predictions issued from the model. The evolutions of the average R_aX of sidewalls engraved at 343 nm for different fluences are displayed in Figure 5. The roughness variation with the pulse to pulse distance confirms the behavior previously pointed out. When shortening the pulse to pulse distance, R_aX reaches a minimum value and then increases due to the deterioration of the sidewall topologic quality. Interestingly, the surface degradation occurring for short pulse to pulse distances has been observed for laser milled pocket bottoms as well [21, 22]. The minimum and maximum values of R_aX, displayed in order to show the surface roughness homogeneity, follow the same trend. Thus, in the following, results are discussed in term of average roughness which is representative of the surface topology. Using the geometrical model presented previously, the sidewall roughness evolution as a function of the pulse to pulse distance *p* is calculated (eq. (5)) and plotted on the same figure (dotted lines). The

value of the crater diameter d_{measur} comes from the average measurement of a crater obtained with 5 single laser pulses. The data have been fitted as well using the same equation and with only one variable, the crater diameter d. The values of d_{fit} given by the fit are larger than d_{measur}. This can be explained by the fact that the fit values result from an indirect measurement realized after a few thousands of laser pulses/area and along a depth of 85 µm. Thus, the crater enlargement can be caused by progressive erosion, shift of the laser spot positioning, decrease of the ablation threshold due to incubation [23], beam defocusing and interaction with the plasma plume.

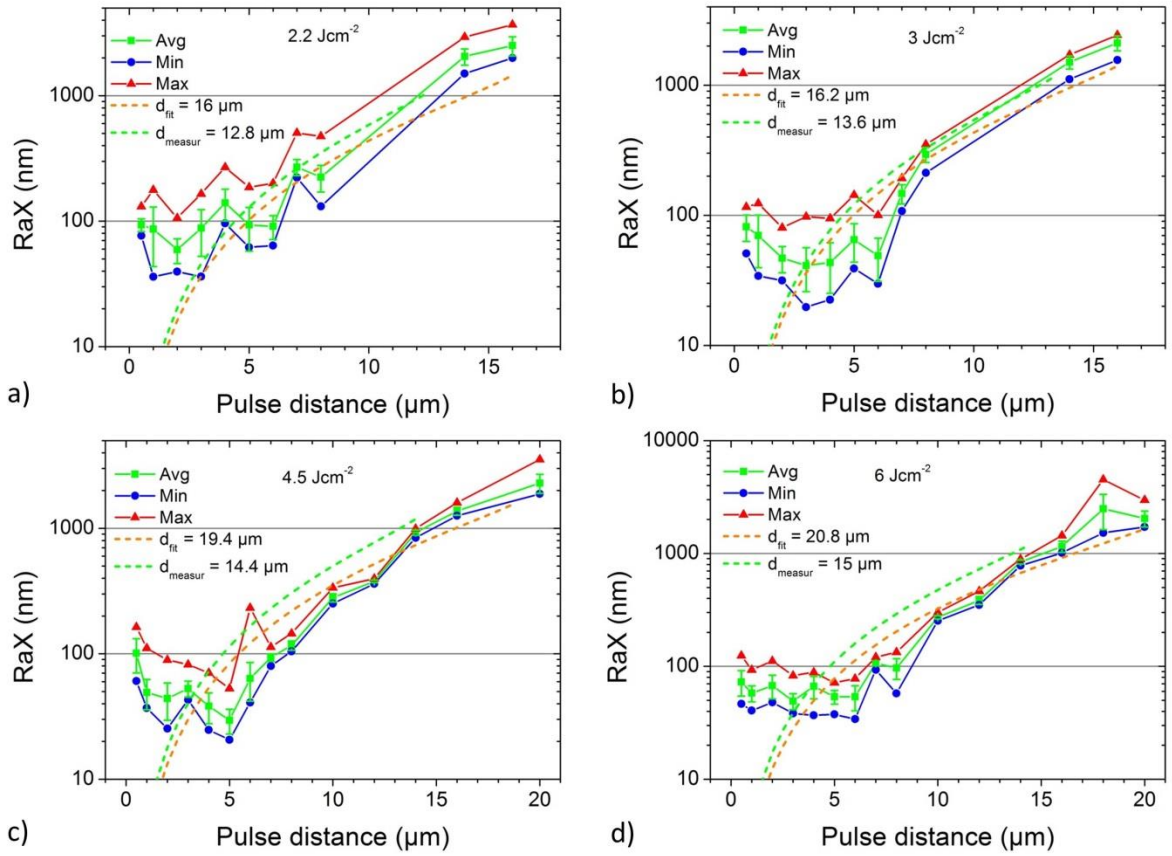

Figure 5 : Sidewall average (Avg), minimum (Min) and maximum (Max) roughness as a function of the pulse to pulse distance after engraving at 343 nm ($\omega_0 \approx 5$ µm, 20 kHz). Avg is obtained by averaging the values of RaX along the whole investigated area between y = 10 and y = 85 µm. Min and Max are the minimum and maximum values of RaX measured in the area. Vertical error bars shown in the figure correspond to the amplitude of the standard deviation. The roughness calculated with the geometrical model and using the crater diameter measurements (d_{measur}) is indicated by the green dashed line. The fit of the data is indicated by the orange dashed line.

Then, the roughness evolution is studied by changing the diameter of the ablation crater. First, the crater size is modified by varying the applied fluence. The evolution of R_aX for different laser fluences and focal spot radii is presented in Figure 6.

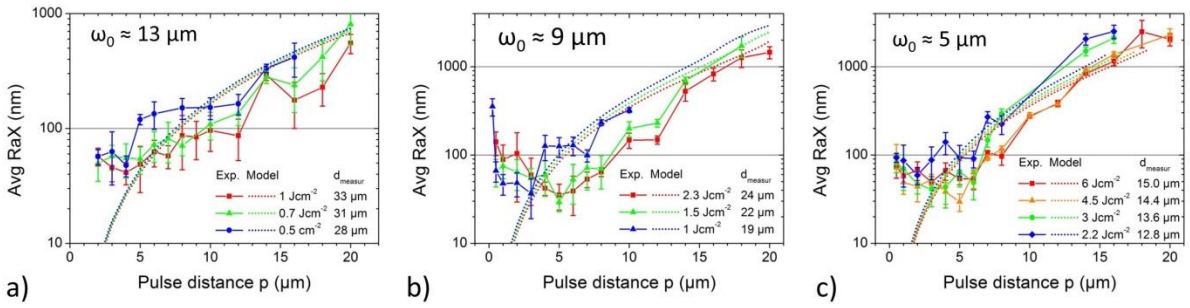

Figure 6 : Sidewall average roughness as a function of the pulse to pulse distance after engraving at 343 nm for different focal spot radii and fluences. Vertical error bars shown in the figure correspond to the amplitude of the standard deviation. The roughness calculated with the geometrical model and using the crater diameter measurements is indicated by the dotted line.

For each focal laser spot radius, two main domains can be defined. In the first domain, pulse to pulse distances >~5 µm, the lowest average roughness (30-40 nm) is obtained by applying the highest fluence, in accordance with the model. Nevertheless, there is no large roughness variation when modifying the fluence. This is explained by the application of fluences much larger than the ablation threshold [17]. In this regime, the fluence variation translates by only a small crater size modification due to a square root and logarithm dependence (see eq. (1)). This is illustrated by the very close dotted lines in Figure 6. In the second domain, p <~5 µm, no clear role of the fluence can be deducted. Therein, the roughness does not evolve in accordance with the geometrical model anymore. The possible reasons of this limitation will be discussed in the section 3.4.

In order to illustrate even more the effect of the crater size, roughness evolutions are compared in Figure 7 by using different focal spot radii and by applying identical fluences. By this way, surfaces engraved by using very different crater diameters can be compared.

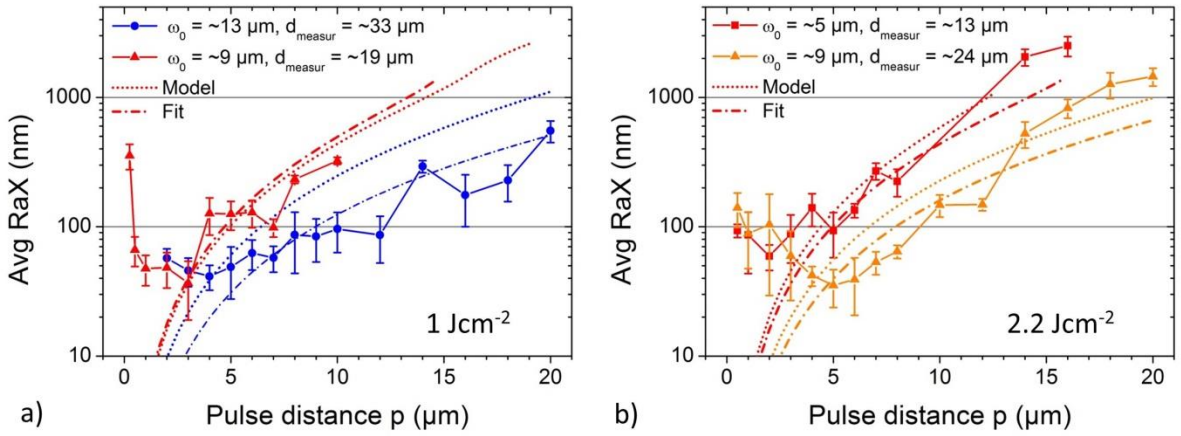

Figure 7 : Sidewall average roughness as a function of the pulse to pulse distance after engraving at 343 nm for different beam waist sizes and 2 fluences: 1 J.cm^{-2} (a) and 2.2 J.cm^{-2} (b). The roughness calculated with the geometrical model and using the crater diameter measurements (d_{measur}) is indicated by the dotted line. The fit of the data is indicated by the dotted and dashed line. Vertical error bars shown in the figure correspond to the amplitude of the standard deviation.

As previously, two clear domains can be defined. For p>~3 µm, for both fluences, the minimum average R_aX is found by using the largest focal spot radius, in accordance with the model. No clear difference can be noticed for p<~3 µm. As the pulse to pulse distance is reduced, the applied fluence plays a less determinant role on the resulting roughness.

The best results achieved at 343 nm and 532 nm are respectively summarized in Table 2 and

Table 3. The lowest roughness values are obtained for an average CO of ~80% for both wavelengths. This specific CO was also obtained in a previous study using a 30 ns UV pulse laser and the Taguchi method to optimize the laser machining parameters [13]. At 343 nm, the minimum roughness is obtained by using the medium focal spot radius (9 µm), in disagreement with the geometrical model. This result has to be relativized as the displayed values, obtained for different CO, are within the standard deviation. In addition, the minima are obtained for short pulse to pulse distances, i.e. in the domain where the roughness does not follow the model.

Table 2 : Minimum average R_aX achieved after engraving at 343 nm and 20 kHz (SD: Standard Deviation).

F (J.cm^{-2})	ω_0 (µm)	Min. avg R_aX (nm)	SD (nm)	Obtained for CO (%)
0.5	13	48	10	85.5
0.66		50	15	93.5
1		41	9	88.0
1	9	37	18	84.2
1.5		29	6	76.9
2.2		35	11	79.0
2.2	5	59	13	84.4
3		41	15	77.9
4.5		30	7	65.3
6		49	8	80.0
Average CO±SD (%)				81±8

Table 3 : Minimum average R_aX achieved after engraving at 532 nm and 30 kHz (SD: Standard Deviation).

F (J.cm^{-2})	Min. avg R_aX (nm)	SD (nm)	Obtained for CO(%)
6	62	15	76.1
4	84	38	84.8
2.6	69	16	62.4
1	71	27	90.4
Average CO±SD (%)			78±12

The lowest roughness is obtained at 343 nm. This may be explained by two reasons. First, the ablation rate is higher at 532 nm due to the large difference of penetration depth [17]. Thus, upon a spot positioning error, the volume of removed matter will be larger at 532 nm, causing a more important deterioration of roughness. The second reason is related to the crater size and its respective optimal CO which limits the minimum inter pulse distance used for engraving. The minimum crater diameters used at 532 and 343 nm were respectively about 31 and 13 µm. Therefore, following the optimal CO (~80%, i.e. $p/r_{crater} \approx 0.4$), the pulse to pulse distance can be reduced down to approximately 2 µm at 343 nm, compared to 6 µm at 532 nm (see Figure 8a). Yet, as a small variation of CO induces a large change of roughness, it is more efficient to reduce the roughness by decreasing the pulse to pulse

distance rather than by increasing the crater size. It can be demonstrated by comparing the derivative of PV (see eq. (3)) calculated in respect to the crater radius *r* and to the pulse to pulse distance *p* (presented in Figure 8b). It can be even shown by equalizing both derivative that abs(dPV/dp)>abs(dPV/dr) below p/r_{crater} = 8/5, i.e. beyond a CO of 20%. Thus, the best results could be obtained at 343 nm. To reduce even more the roughness, it should be interesting to work with smaller focal spot radii, allowing to further decrease the pulse to pulse distance.

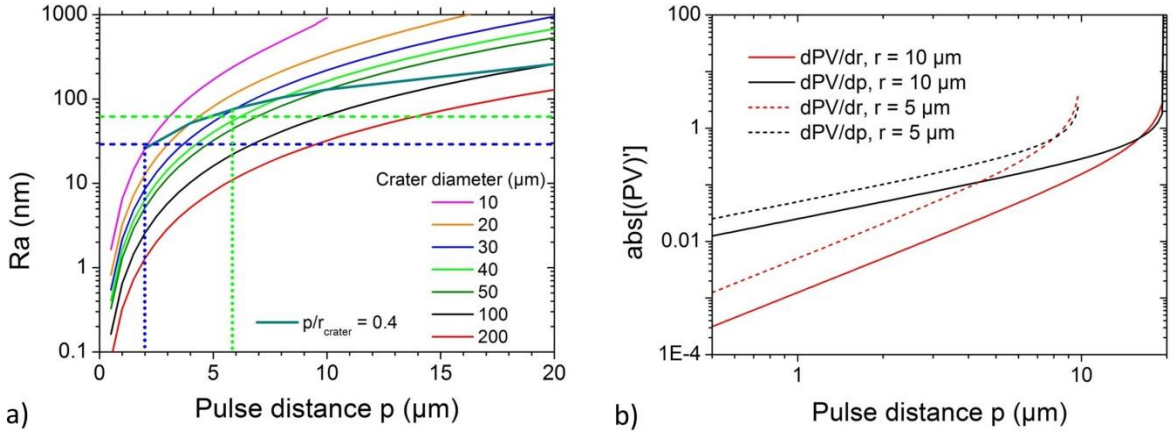

Figure 8 : a) Evolution of the theoretical roughness (R_aX) as a function of the pulse to pulse distance for different crater sizes. The horizontal dashed lines represent the lowest measured roughness at 343 (blue) and 532 nm (green). The dark cyan line represents the theoretical roughness achieved with a ratio p/r_{crater} of 0.4. The vertical dotted lines indicate the optimal pulse distances calculated for the smallest crater sizes used in the experiment. b) Derivative of PV as a function of the pulse distance calculated with a crater radius of 5 (dashed line) and 10 µm (solid line).

3.2. Sidewall roughness (R_aY) and waviness along the beam propagation direction (W_aY)

A typical average Y profile of a sidewall is shown on Figure 9a. Unlike the X profile, the Y profile is curved and can be divided into two parts. The first part, the edge, is mainly due to the progressive erosion of the cavity edge and by the nearly Gaussian spatial distribution of the pulse, inducing a tapering angle and a cone like profile [3, 24]. The second part, i.e. the long range curvature beyond *y* for which the profile height *z* is maximum (labelled Max z in Figure 9a), is caused by the increase of the ablated diameter, mainly determined by the Rayleigh length, with *y*. The curvature amplitude is in the micrometric range and much higher than the short range height variation. Thus, the sidewall roughness can only be rigorously determined after subtracting this curvature, hereafter referred as the waviness W_aY, which strongly depends on the measurement location. Therefore, in order to be able to compare the different experimental results, the values, R_aY and W_aY will be always measured starting from Max z and along a fixed length of 40 µm, after adjustment (see figure 9a). The corrected profile is obtained after subtraction of a polynomial fit of the data. The obtained polynomial is then used for the calculation of the waviness which value is obtained by the same way as the roughness [19].

The roughness measurements are presented in Figure 9b. For short pulse to pulse distances (below 6 µm), R_aY does not show a strong dependence on the fluence and does not vary sensibly with CO. This outcome was expected since a change of pulse to pulse distance should not affect the sidewall roughness along the beam propagation direction. In this range, the CO is large enough to induce a spatially homogeneous ablation for any fluence. However, beyond a certain pulse to pulse distance (~6 to ~10 µm depending on the applied fluence), R_aY increases. This is related to the heterogenization of

the energy spatial distribution as CO decreases. This induces a spatially heterogeneous ablation rate which is accentuated with the distance from the wafer surface. The CO range in which R_aY stays low logically depends on the applied fluence as it determines directly the size of the ablated area.

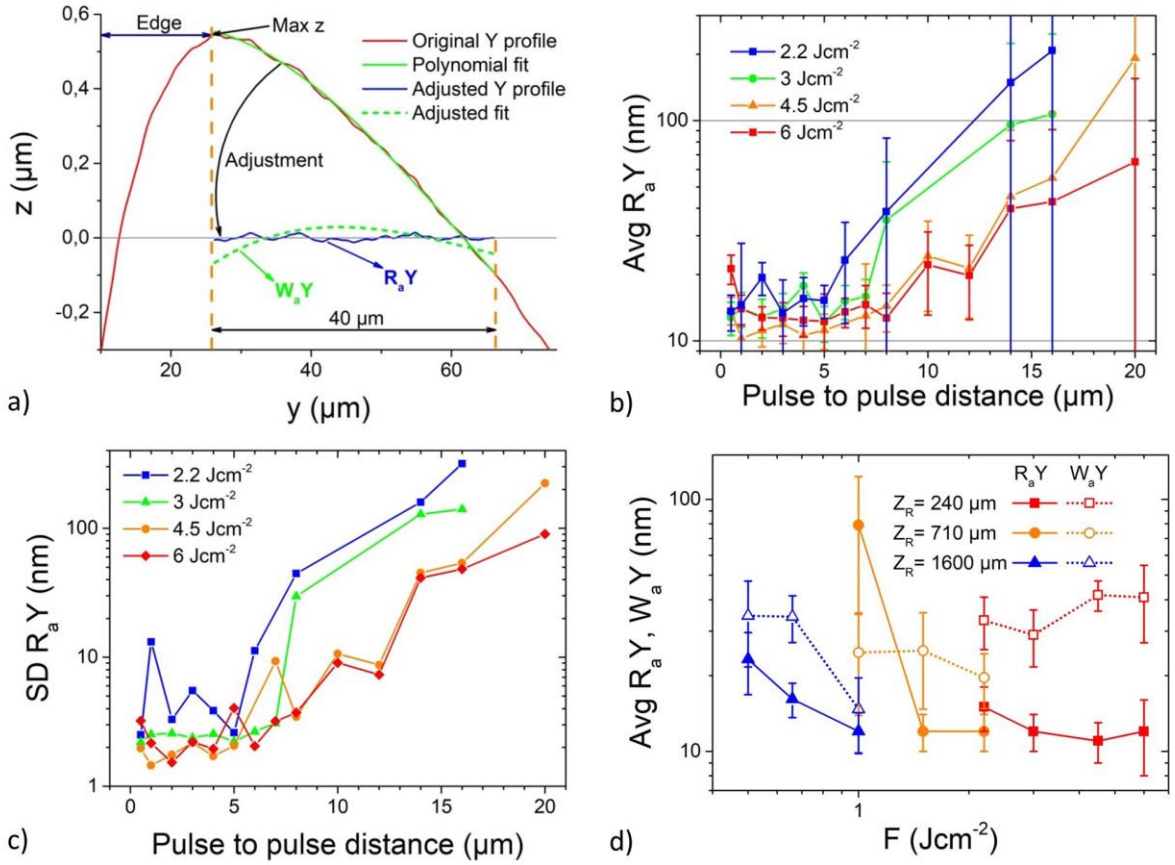

Figure 9 : a) Illustration of the roughness and waviness extraction from a typical sidewall profile. b) Evolution of the sidewall roughness (R_aY) measured along the beam propagation direction (y) with the pulse to pulse distance (343 nm). c) Evolution of the standard deviation with the pulse to pulse distance for different fluences. d) Evolution of the average waviness W_aY and roughness R_aY for a pulse to pulse distance of 5 µm, different Rayleigh lengths and fluences.

In addition, we can notice in Figure 9c that the R_aY standard deviation strongly depends on the pulse to pulse distance with a most homogeneous surface obtained for ~5 µm. Then, when decreasing CO, R_aY becomes more and more heterogeneous. This can be explained by the size variation of the ablated crater due to defocusing, as discussed earlier. This is confirmed by the less dispersed R_aY obtained at high fluence. Concerning the large CO, the dispersion increase of R_aY should be directly related to the sidewall deterioration discussed in section 3.1.

The evolution of R_aY and the waviness W_aY with the fluence and the Rayleigh length is presented in Figure 9d. The larger the fluence, the lower the roughness. This is mainly due to the higher applied energy density which maintains a homogeneous ablation despite the defocusing. This is also explained by the debris which are more present at low fluence as reported in previous experiments [3]. For example, at 1 J.cm^{-2} and Z_R=710 µm, R_aY decreases from 79 nm to 17 nm upon cleaning (data not shown). When the applied fluence is high enough to remove most of the debris (above 1 J.cm^{-2}), R_aY is typically in the 10-20 nm range whatever Z_R (see figure 9d). However, this parameter mainly determines the waviness of the sidewall. In the investigated experimental conditions, W_aY is most

often larger than R_aY and thus, is not negligible for a proper description of the flank, especially if straight walls are desired. Below 1 J.cm^{-2}, despite an equivalent energy input, the sidewall is still in formation, inducing a large waviness (see section 3.3 for details). Above 1 J.cm^{-2}, the waviness increases logically when Z_R decreases due to a stronger defocusing which induces a larger crater size variation.

The roughness values obtained at 343 nm and 532 nm are summarized in Table 4 and 5. The minimum R_aY is obtained for an average CO of 82 and 91% whereas the best roughness homogeneity (minimum standard deviation) is found at 87 and 75% respectively at 343 and 532 nm. Best results are obtained for both wavelengths in the same CO range. Whatever the beam size, the lowest average roughness (14 nm) is systematically obtained by applying the highest fluence (see also Figure 9d). As the sidewalls are characterized without any cleaning after laser processing, this can be explained in part by the presence of nanoparticles produced during the ablation [25]. Indeed, as observed in previous experiments, the higher the fluence the cleaner are the sidewalls [3].

The measured roughness is higher at 532 nm for equivalent applied energy densities (6 J.cm^{-2}). This can be explained by the shorter penetration depth at 343 nm which allows to use more efficiently the pulse energy for cleaning [26] and ablating the asperities of the sidewall surface.

Table 4 : Average R_aY (calculated between *p*=2 and *p*=10 µm), minimum average R_aY, standard deviations (SD) and respective CO for sidewalls engraved at 343 nm and 20 kHz.

ω_0 (µm)	F (J.cm^{-2})	Min. avg R_aY (nm)	SD (nm)	CO %	Min. SD (nm)	CO %	Avg R_aY (nm)	SD (nm)
13	0.5	13	3	92.8	3	89.1	39	28
	0.66	13	2	93.5	2	93.5	23	16
	1	11	1	81.9	1	81.9	14	2
9	1	12	2	94.7	2	94.7	30	22
	1.5	12	2	76.9	2	95.4	16	3
	2.2	12	2	79.0	2	74.8	14	2
5	2.2	13	6	76.6	3	96.1	27	17
	3	12	2	63.2	2	63.2	18	8
	4.5	10	2	93.1	1	93.1	15	6
	6	12	4	66.7	2	86.7	14	3
Average CO±SD (%)			82±12		87±11		-	

Table 5 : Average R_aY (calculated between *p*=2 and *p*=16 µm), minimum average R_aY, standard deviations (SD) and respective CO for sidewalls engraved at 532 nm and 30 kHz.

F (J.cm^{-2})	Min. avg R_aY (nm)	SD (nm)	CO %	Min. SD (nm)	CO %	Avg R_aY (nm)	SD (nm)
6	26	6	88.0	4	66.5	37	8
4	19	9	97.5	6	59.6	54	22
2.6	33	5	83.9	5	83.9	45	7
1	26	31	93.6	6	90.4	84	11
Average CO±SD (%)		91±6		75±14		-	

3.3. Sidewall evolution during laser engraving

Previous sidewalls were engraved with a limited depth just for allowing the roughness measurement along the beam propagation direction on a sufficient length (~85 µm) to be representative. In this paragraph, the evolution of the roughness is investigated when deeper cavities are achieved. SEM images of sidewalls engraved with different numbers of scans are presented in Figure 10. The sidewall morphology varies a lot depending on the depth *y* and the number of scans. The measured roughness increases with the depth *y*, as confirmed by the evolution of R_aX along the sidewall (see Figure 11a). First, R_aX slightly decreases with *y* and then, if the sidewall is still in formation (150 and 200 scans), R_aX increases. Beyond 200 scans, the R_aX evolution does not change significantly. When increasing the number of pulses, the smooth area becomes larger and after a sufficient number of pulses, the sidewall appears homogeneous and smooth from top to bottom of the wafer (see Figure 10 with 900 scans).

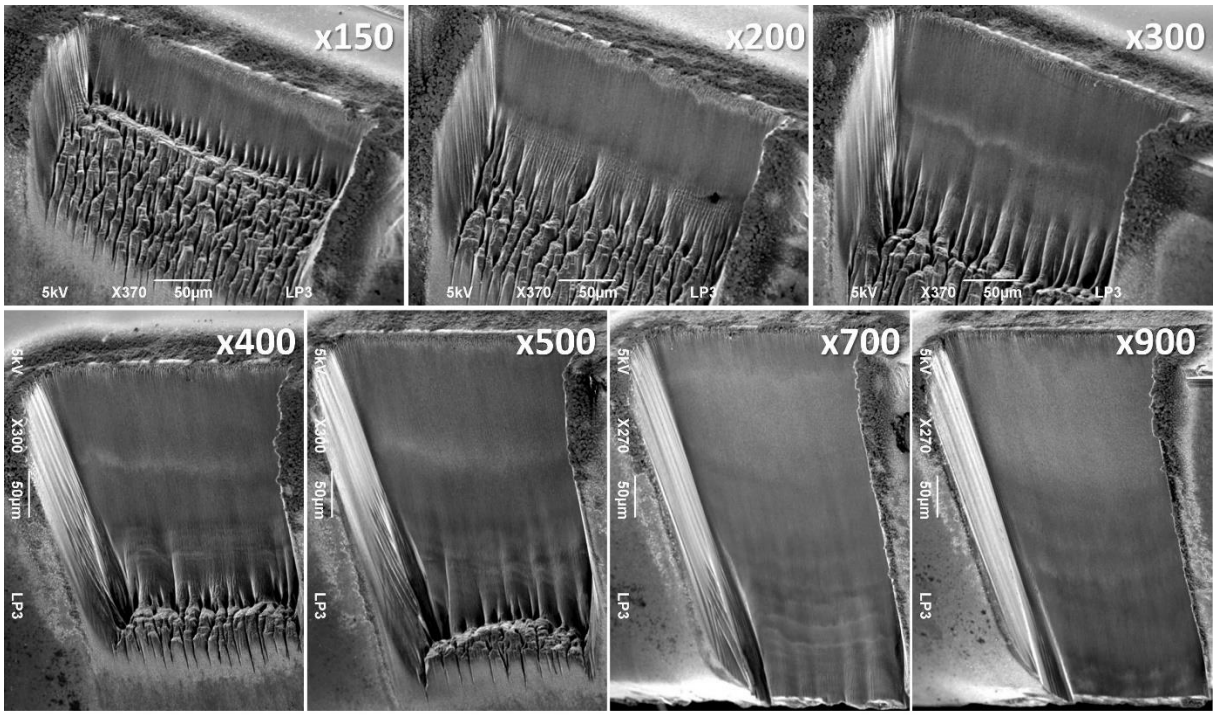

Figure 10 : SEM images of sidewalls engraved in silicon after different number of scans, from 150 to 900 (343 nm, ω_0≈9µm, 2.3 J.cm^{-2}, ~12.2 pulses/area/scan). The sidewalls were cleaned in order to remove debris coming from the underneath substrate.

The evolution of the sidewall average roughness and waviness values during engraving is presented in Figure 11b. At start, both R_aX and R_aY are high because the sidewall is still under formation. Then, when increasing the number of pulses, the roughness decreases and stabilizes. The minimum value of W_aY obtained for 200 scans is caused by the flattening of the profile (red solid line in Figure 11c). Then, when increasing the number of scans, the curvature accentuates. After a few hundreds of scans, there is no noticeable change of the sidewall roughness and the Y profiles become stable (see the superimposed curves beyond 400 scans in Figure 11c). At this point, increasing the number of pulses is useless because the final geometrical shape, mainly determined by Z_R, has been reached. As R_aX is large compared to R_aY, the best compromise for optimizing the surface roughness can be found by following the evolution of R_aX. The optimal is reached for about 500 scans. Beyond, the surface quality does not change significantly.

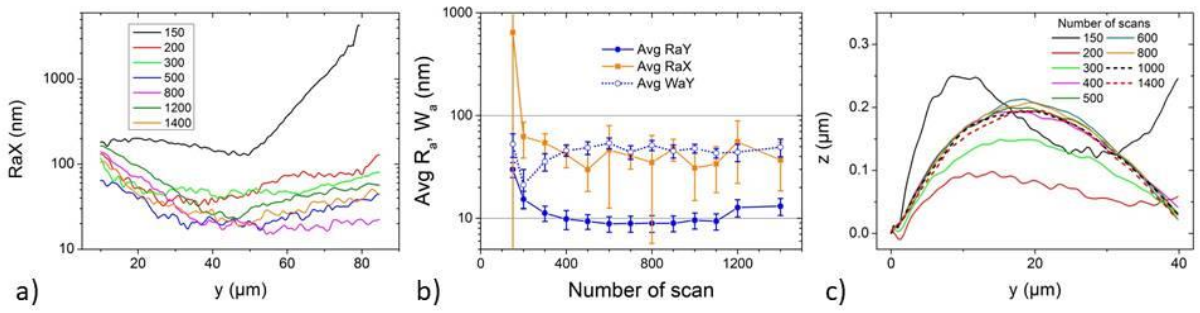

Figure 11 : a) Evolution of R_aX along the sidewall for different number of scan (343 nm, $\omega_0 \approx 9\mu m$, 2.3 J.cm^{-2}, ~12.2 pulses/area/scan). b) Average sidewall roughness and waviness as a function of the number of scan. c) Average Y profile for different number of scans.

3.4. Sidewall smoothing limitations

According to the geometrical model, R_aX should reach the nanometer level when the pulse to pulse distance is short enough (see Figure 2b). But our experimental results demonstrated a disagreement and limitations.

Many factors may be involved in these limitations. First, achieving such a low roughness requires a very precise spot positioning of the scanner. Some tests revealed that the spots are not perfectly overlapped from one pass to another. According to the manufacturer, the scanner positioning repeatability and noise are below 2 and 5 µrad, which translates by a maximum shift of 320 nm and 800 nm respectively on the focal plane. Thus, it seems not surprising to be not able of smoothing the sidewall to the nanometer scale. However, this factor is not overlap dependent. On the contrary, when working with large overlap, low scanning velocities are used, which should reduce the spot positioning errors. Thus, this factor can explain a roughness stability but not a degradation when increasing CO (Fig. 5 and 6).

Another factor involves the debris. The machining conditions were chosen to limit the debris redeposition on the sidewalls but, as they are not cleaned by a post treatment, some nanoparticles may remain and deteriorate the roughness. Moreover, the presence of debris on the flank is strongly dependent on the repetition rate, fluence and scanning speed [3]. In some cases, they accumulate on the edge and scatter the laser beam, inducing a curtaining effect of the sidewall, as observed in Figure 3 and Figure 4. In addition, using a typical repetition rate of 20 kHz, beam interaction with the slowest particles (~10^4 cm/s) of the previous generated ablation plume is possible [27, 28], leading to beam

quality deterioration and thus heterogeneous machining of the sidewall. This factor may be one of the most relevant as the importance of the interaction with the particles is directly related with CO. Indeed, the shorter the pulse to pulse distance, the more direct will be the interaction between the laser beam and the previous induced plume, deteriorating more the quality of the laser beam before interacting with the sample. Moreover, typical formation and lifetime of the plasma plume was shown to be about 20 ps and a few µs respectively [29, 30]. Therefore, the beam is even interacting with the plume during the laser pulse, which adds a source of beam degradation.

The last factor is related to the repartition of the energy density. In our experiment, when changing CO, the number of pulses per area is kept constant by varying the number of pass, but the energy distribution at the crater scale is different (see Figure 12). The total received energy by the material is the same but is used differently. Indeed, when the inter pulse distance is reduced, the beam interacts with a larger modified surface during the first pass. This leads to a more heterogeneous reflectivity and absorption of the laser, creating a highly rough surface, despite a homogeneous energy density distribution (flat profiles noticeable for overlaps larger than 60% in Figure 12). This method, i.e. laser induced texturing performed with a very large CO [31], is used to produce highly absorbing structures. This kind of surface roughening, amplified by the high number of pulses required for deep engraving [21, 32], should affect the sidewall surface topography as well. As this factor is pulse to pulse distance dependent, it should be relevant to understand the surface deterioration occurring for large CO. If this explanation is confirmed, it will be difficult to reduce more the surface roughness.

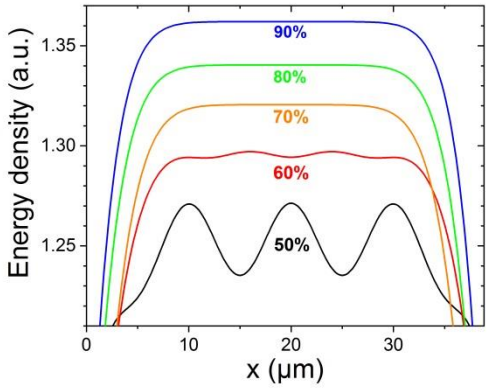

Figure 12 : Energy density profiles resulting of the superimposition of Gaussian functions calculated for different pulse overlaps (from 5 to 28 Gaussians for overlaps between respectively 50% and 90%, taking ω_0=10 µm). Curves have been translated to facilitate the reading.

4. Conclusion

The surface roughness of laser micromachined sidewalls in silicon were investigated theoretically and experimentally. R_aX, which is the roughness measured along the scanning beam direction, can be minimized by increasing CO and the crater size, in accordance with a simple geometrical model. Experimentally, the minimum R_aX is obtained for a CO of ~80% and the largest crater sizes. Beyond 80%, the roughness degradation is probably due to two main phenomena. The first involves the interaction between the laser beam and ablation plume (both direct and previous ones), which deteriorates the beam propagation. The second is related to the highly heterogeneous ablation occurring for large overlaps, which induces a rough surface. Along the beam propagation direction, the

sidewall is characterized by a relatively high waviness (W_aY) which induces a more important height variation than the roughness. The waviness depends mainly on the Rayleigh length. Thus, W_aY can be reduced by using a large focal spot radius and a short wavelength. Once the sidewall is finished, the surface topology does not vary much with the laser micromachining time. Overall, smooth and homogeneous surfaces can be produced by choosing a CO close to 80%. The best results were obtained at a laser wavelength of 343 nm, which allows to extend the Rayleigh zone, to increase the laser absorption on the sidewall asperities and to improve the induced cleaning thanks to a more confined interaction.

This approach allows the roughness tuning of laser micromachined sidewalls. As it is based on a geometrical model, it is extendable to other materials as long as the surface melting, which may erase the induced periodic structuring, is not significant. This tuning possibility can be useful to modify the surface properties, such as reflectivity, friction and wettability, and therefore adapt the sidewall to different applications.

Acknowledgements

This work has been carried out thanks to the support of the A*MIDEX project (n° ANR-11-IDEX-0001-02) funded by the « Investissements d'Avenir » French Government program, managed by the French National Research Agency (ANR).

References

[1] K. Sugioka, Y. Cheng, Ultrafast lasers—reliable tools for advanced materials processing, Light: Science &Amp; Applications, 3 (2014) e149.
[2] D. Tan, K.N. Sharafudeen, Y. Yue, J. Qiu, Femtosecond laser induced phenomena in transparent solid materials: Fundamentals and applications, Progress in Materials Science, 76 (2016) 154-228.
[3] A. Sikora, L. Fares, J. Adrian, V. Goubier, A. Delobbe, A. Corbin, M. Sentis, T. Sarnet, Picosecond laser micromachining prior to FIB milling for electronic microscopy sample preparation, Applied Surface Science, 418 (2017) 607-615.
[4] S. Jung, P.A. Lee, B.H. Kim, Surface polishing of quartz-based microfluidic channels using CO2 laser, Microfluidics and Nanofluidics, 20 (2016) 84.
[5] D.H. Kam, L. Shah, J. Mazumder, Femtosecond laser machining of multi-depth microchannel networks onto silicon, Journal of Micromechanics and Microengineering, 21 (2011) 045027.
[6] M. Stolze, T. Herrmann, J.A. L'huillier, Fabrication of low-loss ridge waveguides in z-cut lithium niobate by combination of ion implantation and UV picosecond laser micromachining, in: SPIE OPTO, SPIE, 2016, pp. 7.
[7] X. Qiangfei, F.M. Patrick, G. He, Y.C. Stephen, Ultrafast and selective reduction of sidewall roughness in silicon waveguides using self-perfection by liquefaction, Nanotechnology, 20 (2009) 345302.
[8] K.H. Oh, J.B. Park, S.I. Cho, H.D. Im, S.H. Jeong, Investigation of sidewall roughness of the microgrooves manufactured with laser-induced etching technique, Applied Surface Science, 255 (2009) 9835-9839.
[9] N. Sudani, K. Venkatakrishnan, B. Tan, Laser singulation of thin wafer: Die strength and surface roughness analysis of 80 µm silicon dice, Optics and Lasers in Engineering, 47 (2009) 850-854.
[10] M. Domke, B. Egle, G. Piredda, S. Stroj, G. Fasching, M. Bodea, E. Schwarz, Ultrashort pulse laser dicing of thin Si wafers: the influence of laser-induced periodic surface structures on the backside breaking strength, Journal of Micromechanics and Microengineering, 26 (2016) 115004.
[11] S.Y. Chou, Q. Xia, Improved nanofabrication through guided transient liquefaction, Nature Nanotechnology, 3 (2008) 295.
[12] S.C. Hung, E.Z. Liang, C.F. Lin, Silicon Waveguide Sidewall Smoothing by KrF Excimer Laser Reformation, Journal of Lightwave Technology, 27 (2009) 887-892.
[13] T.P. Pusch, M. D'Auria, N. Tolou, A.S. Holmes, Laser Micromachining of Thin Beams for Silicon MEMS: Optimization of Cutting Parameters Using the Taguchi Method, (2015) V004T009A031.
[14] M. Kagerer, F. Irlinger, T.C. Lueth, Laser source independent basic parameters — Focus position, pulse overlap, track overlap — In laser micro milling using as rapid manufacturing process, in: 2012 IEEE/ASME International Conference on Advanced Intelligent Mechatronics (AIM), 2012, pp. 135-140.
[15] J.M. Bovatsek, R.S. Patel, Highest-speed dicing of thin silicon wafers with nanosecond-pulse 355nm q-switched laser source using line-focus fluence optimization technique, in: SPIE LASE, SPIE, 2010, pp. 12.
[16] V. Krishnan, S. Nitin, T. Bo, A high-repetition-rate femtosecond laser for thin silicon wafer dicing, Journal of Micromechanics and Microengineering, 18 (2008) 075032.
[17] A. Sikora, D. Grojo, M. Sentis, Wavelength scaling of silicon laser ablation in picosecond regime, Journal of Applied Physics, 122 (2017) 045702.

[18] J.M. Liu, Simple technique for measurements of pulsed Gaussian-beam spot sizes, Opt. Lett., 7 (1982) 196-198.
[19] ISO, Geometrical Product Specifications (GPS) — Surface texture: Profile method — Terms, definitions and surface texture parameters, in, 1997.
[20] N. Sanner, O. Utéza, B. Bussiere, G. Coustillier, A. Leray, T. Itina, M. Sentis, Measurement of femtosecond laser-induced damage and ablation thresholds in dielectrics, Applied Physics A, 94 (2009) 889-897.
[21] S. Lee, D. Yang, S. Nikumb, Femtosecond laser micromilling of Si wafers, Applied Surface Science, 254 (2008) 2996-3005.
[22] J. Cheng, W. Perrie, S.P. Edwardson, E. Fearon, G. Dearden, K.G. Watkins, Effects of laser operating parameters on metals micromachining with ultrafast lasers, Applied Surface Science, 256 (2009) 1514-1520.
[23] P.M. Fauchet, Gradual surface transitions on semiconductors induced by multiple picosecond laser pulses, Physics Letters A, 93 (1983) 155-157.
[24] O.V. Borisov, X. Mao, R.E. Russo, Effects of crater development on fractionation and signal intensity during laser ablation inductively coupled plasma mass spectrometry, Spectrochimica Acta Part B: Atomic Spectroscopy, 55 (2000) 1693-1704.
[25] S. Amoruso, G. Ausanio, A.C. Barone, R. Bruzzese, L. Gragnaniello, M. Vitiello, X. Wang, Ultrashort laser ablation of solid matter in vacuum: a comparison between the picosecond and femtosecond regimes, Journal of Physics B: Atomic, Molecular and Optical Physics, 38 (2005) L329.
[26] L. Yong-Feng, S. Wen-Dong, T. Chong-Kiat, C. Daniel Siu-Hung, L. Teck-Seng, Wavelength Effects in the Laser Cleaning Process, Japanese Journal of Applied Physics, 37 (1998) 840.
[27] S. Amoruso, G. Ausanio, R. Bruzzese, L. Gragnaniello, L. Lanotte, M. Vitiello, X. Wang, Characterization of laser ablation of solid targets with near-infrared laser pulses of 100fs and 1ps duration, Applied Surface Science, 252 (2006) 4863-4870.
[28] S. Bruneau, J. Hermann, G. Dumitru, M. Sentis, E. Axente, Ultra-fast laser ablation applied to deep-drilling of metals, Applied Surface Science, 248 (2005) 299-303.
[29] W. Marine, J.M.S. D'Aniello, J. Marfaing, Picosecond YAG laser photoablation of amorphous silicon, Applied Surface Science, 46 (1990) 239-244.
[30] J. König, S. Nolte, A. Tünnermann, Plasma evolution during metal ablation with ultrashort laser pulses, Opt. Express, 13 (2005) 10597-10607.
[31] M. Halbwax, T. Sarnet, P. Delaporte, M. Sentis, H. Etienne, F. Torregrosa, V. Vervisch, I. Perichaud, S. Martinuzzi, Micro and nano-structuration of silicon by femtosecond laser: Application to silicon photovoltaic cells fabrication, Thin Solid Films, 516 (2008) 6791-6795.
[32] T. Sarnet, From black silicon to photovoltaic cells, using short pulse lasers, AIP Conference Proceedings, 1464 (2012) 219-228.